

## ***n*-sided polygonal hybrid finite elements involving element boundary integrals only for anisotropic thermal analysis**

R. F. CAO<sup>1)</sup>, X. J. ZHAO<sup>2)</sup>, W. Q. LIN<sup>3)</sup>, H. WANG<sup>3)</sup>

<sup>1)</sup>*School of Traffic Engineering, Huanghe Jiaotong University, Jiaozuo, China, 454950*

<sup>2)</sup>*Henan Province Engineering Laboratory for High Temperature and Wear Materials, School of Material Science & Engineering, Henan University of Technology, Zhengzhou, China, 450001*

<sup>3)</sup>*College of Civil Engineering, Henan University of Technology, Zhengzhou, China, 450001, e-mails: wanqinglin@stu.haut.edu.cn, huiwang@haut.edu.cn*

AS A COMBINATION OF THE TRADITIONAL FINITE ELEMENT METHOD AND BOUNDARY ELEMENT METHOD, the *n*-sided polygonal hybrid finite element method with fundamental solution kernels, named as HFS-FEM, is thoroughly studied in this work for two-dimensional heat conduction in fully anisotropic media. In this approach, the unknown temperature field within the polygon is represented by the linear combination of anisotropic fundamental solutions of problem to achieve the local satisfaction of the related governing equations, but not the specific boundary conditions and the continuity conditions across the element boundary. To tackle such a shortcoming, the frame temperature field is independently defined on the entire boundary of the polygonal element by means of the conventional one-dimensional shape function interpolation. Subsequently, by the hybrid functional with the assumed intra- and inter-element temperature fields, the stiffness equation can be obtained including the line integrals along the element boundary only, whose dimension is reduced by one compared to the domain integrals in the traditional finite elements. This means that the higher computing efficiency is expected. Moreover, any shaped polygonal elements can be constructed in a unified form with the same fundamental solution kernels, including convex and non-convex polygonal elements, to provide greater flexibility in meshing effort for complex geometries. Besides, the element boundary integrals endow the method higher versatility with a non-conforming mesh in the pre-processing stage of the analysis over the traditional FEM. No modification to the HFS-FEM formulation is needed for the non-conforming mesh and the element containing hanging nodes is treated normally as the one with more nodes. Finally, the accuracy, convergence, computing efficiency, stability of non-convex element, and straightforward treatment of non-conforming discretization are discussed for the present *n*-sided polygonal hybrid finite elements by a few applications in the context of anisotropic heat conduction.

**Key words:** hybrid finite element, polygon, non-conforming mesh, fundamental solution, anisotropic material, heat conduction.

## 1. Introduction

HEAT CONDUCTION IN FULLY ANISOTROPIC MATERIALS has received much more attention in engineering, especially for the extensive applications of composite materials, which generally consist of fillers and matrix materials and involve complex microstructures. Although many attempts have been made in solving anisotropic heat conduction by the theoretical methods [1–3], it is difficult to deal with anisotropic structures with complex material definitions, boundary shapes or boundary conditions. Accordingly, various numerical methods have been resorted to for serving this purpose, including finite element method (FEM) [4, 5], boundary element method (BEM) [6–9], meshless method [10–12], hybrid Trefftz element method (HT-FEM) [13, 14], scaled boundary finite element method [15], etc.

Among various numerical methods, the FEM and BEM are the ubiquitous choice to solve such boundary-value problems in anisotropic solids. For the FEM, the unitary polynomial interpolation of temperature variable is introduced over the entire element level, instead of the whole solution domain, so that it can be applied for multi-material issues flexibly. However, to meet the conforming requirements, the construction of shape functions becomes tedious and generally different types of elements require different forms of shape functions. Besides, the time-consuming domain integration is unavoidable. Moreover, the model having local holes, cracks, or concentrated heat sources needs mesh refinement, which leads to a significant increase in the amount of calculation of the model. Such limitations are encountered to the recently developed polygonal finite elements too [16–18]. For the BEM, the complex theory background such as the derivation of boundary integral equation from Green’s second identity is required. Moreover, it easily encounters difficulties in dealing with singular and super singular integrals. Besides, the final solution matrix is full, so the computational efficiency issue becomes considerable for problems with a large amount of local defects or multiple material constituents.

Typically, as a hybrid method combining the advantages of FEM and BEM, the hybrid finite element formulation with approximating kernels of fundamental solutions of a problem, named as HFS-FEM in literature [19], has been extensively developed for isotropic thermal and elastic analyses [20–27]. In the HFS-FEM, the fundamental solutions at different source points are employed as kernel functions for approximating the element interior field, which exactly satisfies the corresponding governing equations, but not the specific boundary conditions and the interfacial continuity conditions across the element boundary. To enforce them, a conforming approximation with conventional shape functions is independently defined along the element boundary. The substitution of them into the hybrid functional in a weak form leads to the element stiffness equation,

which includes element boundary integrals only in computation. Obviously, the integration dimension is reduced by one compared to the domain integrals in the traditional finite elements. More importantly, the element boundary integration strategy makes that hybrid element with any numbers of sides (*n*-sided polygonal element) can be constructed in a unified form with the same fundamental solution kernels, including convex and non-convex polygonal elements, to provide great flexibility in automatic meshing manipulation to complex geometries. Besides, the element boundary integrals endow the method higher versatility with non-conforming mesh in the pre-processing stage of analysis, compared to the FEM. This appealing feature is beneficial to adaptive mesh refinement, where a straightforward subdivision of individual polygonal element usually results in hanging nodes, as displayed in Fig. 1. A non-conforming mesh containing hanging nodes can be handled in the HFS-FEM in a straightforward way, because the HFS-FEM simply interprets a hanging node in a non-conforming mesh as a division of an edge, and as a result, the number of edges in the element sharing this node increase by one. This operation requires no modification to the HFS-FEM formulation and the element is treated normally. More important, the special fundamental solutions satisfying the local constraints can be used to construct specially-purposed elements, i.e. special hole element, special inclusion element, as illustrated in [20, 22, 23, 25], which can extremely reduce the meshing and computing effort around the local defects.

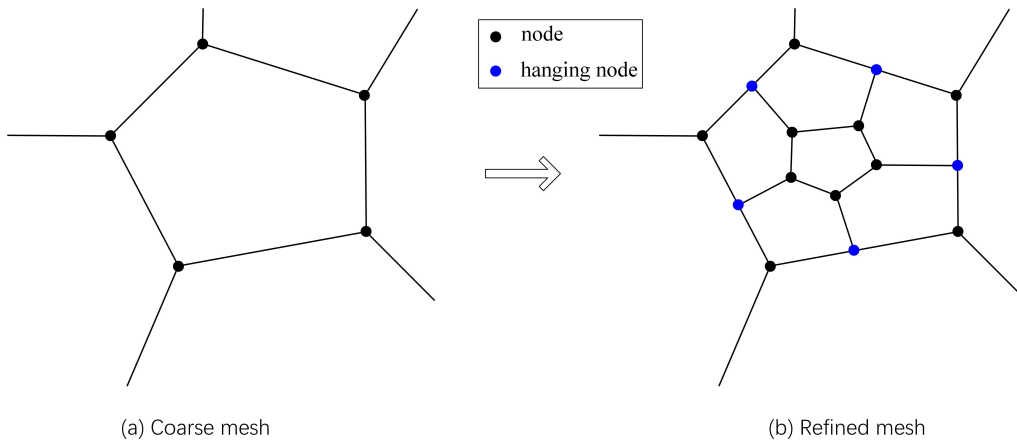


FIG. 1. Schematic of subdivision of a polygonal element with hanging nodes.

It is worth pointing out that the HFS-FEM formulation is different from the HT-FEM, which uses a series of T-complete solutions satisfying the governing equation of the problem to represent the interior approximation [28–33]. However, it is observed that the required T-complete solutions are difficult to

be derived for most of physical problems. Moreover, T-complete functions typically are power functions of the distance variable  $r$ , so the exponential growth of T-complete functions will commonly give an ill-conditioned system of equations.

In this paper, a two-dimensional steady-state heat conduction in fully anisotropic solids is extendedly studied using the  $n$ -sided polygonal hybrid finite element method with flexible conforming or non-conforming, convex or non-convex polygon discretization. The main novelty of this work comes from the employment of the anisotropic fundamental solutions to achieve the exact satisfaction of the anisotropic governing equations of heat conduction, and then the one-dimensional line integrals over the element boundary for the computation of element stiffness matrix, which greatly serve the construction of arbitrarily shaped polygonal element and the improvement of computational efficiency. Also, the role of polygon-shaped hybrid finite elements would be strengthened in the analysis by the simple and straightforward refinement manipulation, as shown in Fig. 1. Besides, it is worth noting that the present method can be easily adapted for the three-dimensional problems in the same theoretical framework given that the three-dimensional fundamental solutions and the two-dimensional shape functions are introduced for approximating the intra- and inter-element fields, respectively. As a result, the two-dimensional area integrals along the element boundary are involved for computing the element stiffness matrix.

The paper is organized as follows: in Section 2, the basic equations of anisotropic heat conduction including the governing equations and the fundamental solutions are briefly reviewed, and then the  $n$ -sided element construction over arbitrary polygons is described in Section 3. In Section 4, three examples are numerically solved by the present element to address the computing properties of the present element. Finally, some conclusions are presented in Section 5.

## 2. Basic equations of anisotropic heat conduction

### 2.1. Governing equations

Consider a bounded domain  $\Omega$  with boundary  $\Gamma$  in two-dimensional space  $\mathbb{R}^2$  with refer to a Cartesian coordinate system  $ox_1x_2$ , as shown in Fig. 2. The generalized partial differential equation governing steady-state heat conduction behavior at arbitrary point  $\mathbf{x} = (x_1, x_2) \in \Omega$  in homogeneous anisotropic solids is expressed as

$$(2.1) \quad k_{11} \frac{\partial^2 T(\mathbf{x})}{\partial x_1^2} + 2k_{12} \frac{\partial^2 T(\mathbf{x})}{\partial x_1 \partial x_2} + k_{22} \frac{\partial^2 T(\mathbf{x})}{\partial x_2^2} = 0$$

where  $T$  is the unknown temperature variable.  $k_{ij} > 0$  denote the general anisotropic thermal conductivities satisfying the Onsager symmetry relation  $k_{12} = k_{21}$  and the positive definite condition  $\Lambda = k_{11}k_{22} - k_{12}^2 > 0$ .

To keep the problem solvable, the following boundary conditions are considered

$$(2.2) \quad \begin{cases} T = \bar{T} & \text{on } \Gamma_T, \\ q_n = \bar{q} & \text{on } \Gamma_q, \\ q_n = h_c(T - T_c) & \text{on } \Gamma_c \end{cases}$$

where  $q_n$  denotes the normal heat flux defined on the boundary.  $\bar{T}$  and  $\bar{q}$  are specified values given on the temperature boundary  $\Gamma_T$  and the heat flux boundary  $\Gamma_q$ , respectively.  $\Gamma_c$  is the convection boundary part, and  $h_c$  denotes the convection coefficient,  $T_c$  is the surrounding temperature.  $\Gamma_T \cup \Gamma_q \cup \Gamma_c = \Gamma$  and  $\Gamma_T \cap \Gamma_q = \emptyset$ ,  $\Gamma_q \cap \Gamma_c = \emptyset$ ,  $\Gamma_T \cap \Gamma_c = \emptyset$ .

Based on Fourier's law, the heat flux components  $q_i$  ( $i = 1, 2$ ) at the arbitrary point  $\mathbf{x}$  can be defined as

$$(2.3) \quad \begin{Bmatrix} q_1(\mathbf{x}) \\ q_2(\mathbf{x}) \end{Bmatrix} = - \begin{bmatrix} k_{11} & k_{12} \\ k_{12} & k_{22} \end{bmatrix} \begin{Bmatrix} \frac{\partial T(\mathbf{x})}{\partial x_1} \\ \frac{\partial T(\mathbf{x})}{\partial x_2} \end{Bmatrix},$$

so that the normal heat flux can be given by

$$(2.4) \quad q_n(\mathbf{x}) \equiv q_1(\mathbf{x})n_1 + q_2(\mathbf{x})n_2 = - \{n_1 \ n_2\} \begin{bmatrix} k_{11} & k_{12} \\ k_{12} & k_{22} \end{bmatrix} \begin{Bmatrix} \frac{\partial T(\mathbf{x})}{\partial x_1} \\ \frac{\partial T(\mathbf{x})}{\partial x_2} \end{Bmatrix}$$

where  $n_i$  are components of the unit outward normal vector  $\mathbf{n}$  to the boundary, as indicated in Fig. 2.

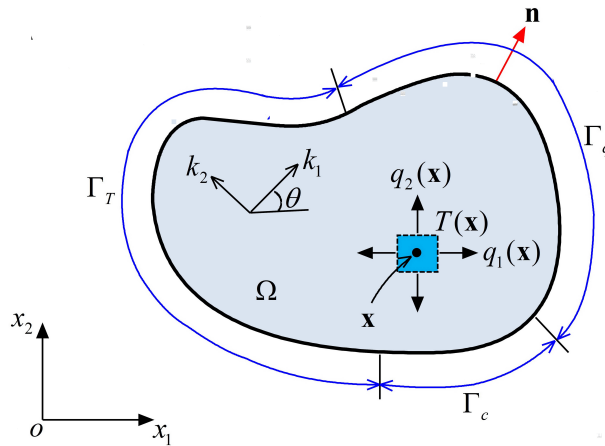


FIG. 2. Schematic of anisotropic heat condition in a bounden domain.

Particularly, for orthotropic materials with two principal directions, which have a ply angle  $\theta$  to the global  $x_1$ -axis, as depicted in Fig 2, the relation between the orthotropic parameters  $k_i$  ( $i = 1, 2$ ) and the generalized anisotropic parameters  $k_{ij}$  ( $i, j = 1, 2$ ) can be given by [34]

$$(2.5) \quad \begin{bmatrix} k_{11} & k_{12} \\ k_{12} & k_{22} \end{bmatrix} = \begin{bmatrix} \cos \theta & \sin \theta \\ -\sin \theta & \cos \theta \end{bmatrix}^T \begin{bmatrix} k_1 & 0 \\ 0 & k_2 \end{bmatrix} \begin{bmatrix} \cos \theta & \sin \theta \\ -\sin \theta & \cos \theta \end{bmatrix}$$

or

$$(2.6) \quad \begin{bmatrix} k_1 & 0 \\ 0 & k_2 \end{bmatrix} = \begin{bmatrix} \cos \theta & \sin \theta \\ -\sin \theta & \cos \theta \end{bmatrix} \begin{bmatrix} k_{11} & k_{12} \\ k_{12} & k_{22} \end{bmatrix} \begin{bmatrix} \cos \theta & \sin \theta \\ -\sin \theta & \cos \theta \end{bmatrix}^T.$$

## 2.2. Anisotropic fundamental solutions

For two-dimensional heat conduction in a fully anisotropic material with thermal conductivities  $k_{ij}$  ( $i, j = 1, 2$ ), the temperature fundamental solution of the problem is defined as the induced temperature response at arbitrary field point  $\mathbf{x}$  in an infinite two-dimensional space  $\mathbb{R}^2$  when a unit point heat source is applied at a source point  $\mathbf{y} \in \mathbb{R}^2$ . This means that the caused temperature distribution represented as  $T^*(\mathbf{x}, \mathbf{y})$  is the solution of the following partial differential equation

$$(2.7) \quad k_{11} \frac{\partial^2 T^*(\mathbf{x}, \mathbf{y})}{\partial x_1^2} + 2k_{12} \frac{\partial^2 T^*(\mathbf{x}, \mathbf{y})}{\partial x_1 \partial x_2} + k_{22} \frac{\partial^2 T^*(\mathbf{x}, \mathbf{y})}{\partial x_2^2} + \delta(\mathbf{x}, \mathbf{y}) = 0, \quad \mathbf{x}, \mathbf{y} \in \mathbb{R}^2$$

where  $\delta(\mathbf{x}, \mathbf{y})$  is Dirac's delta function satisfying the following property

$$(2.8) \quad \int_{\Omega} h(\mathbf{x}) \delta(\mathbf{x}, \mathbf{y}) d\Omega = \begin{cases} h(\mathbf{y}) & \text{for } \mathbf{y} \in \Omega, \\ 0 & \text{for } \mathbf{y} \notin \Omega. \end{cases}$$

Obviously, the temperature solution of Eq. (2.7) is defined everywhere except when the source point  $\mathbf{y}$  coincides with the field point  $\mathbf{x}$ , where it is singular. Thus the source point  $\mathbf{y}$  is sometimes called the singularity. In order to obtain this solution, the Fourier transform or Radon transform can be applied on both sides of Eq. (2.7), and the concentrated excitation is reproduced by the contour integral in the neighborhood of the source point  $\mathbf{y}$  [35, 36]. As a result, the temperature fundamental solution can be written as

$$(2.9) \quad T^*(\mathbf{x}, \mathbf{y}) = -\frac{1}{2\pi\sqrt{\Lambda}} \ln R$$

in which  $R$  is the geodesic distance between  $\mathbf{x}$  and  $\mathbf{y}$

$$(2.10) \quad R = \sqrt{k_{22}r_1^2 - 2k_{12}r_1r_2 + k_{11}r_2^2}$$

with  $r_i = x_i - y_i$  ( $i = 1, 2$ ) and  $\mathbf{y} = (y_1, y_2)$ .

Subsequently, the derivatives of the induced temperature field can be given by

$$(2.11) \quad \begin{aligned} \frac{\partial T^*(\mathbf{x}, \mathbf{y})}{\partial x_1} &= -\frac{1}{2\pi\sqrt{\Lambda}} \frac{k_{22}r_1 - k_{12}r_2}{R^2}, \\ \frac{\partial T^*(\mathbf{x}, \mathbf{y})}{\partial x_2} &= -\frac{1}{2\pi\sqrt{\Lambda}} \frac{k_{11}r_2 - k_{12}r_1}{R^2}, \end{aligned}$$

from which the induced heat flux components can be written as

$$(2.12) \quad \begin{Bmatrix} q_1^*(\mathbf{x}, \mathbf{y}) \\ q_2^*(\mathbf{x}, \mathbf{y}) \end{Bmatrix} = - \begin{bmatrix} k_{11} & k_{12} \\ k_{12} & k_{22} \end{bmatrix} \begin{Bmatrix} \frac{\partial T^*(\mathbf{x}, \mathbf{y})}{\partial x_1} \\ \frac{\partial T^*(\mathbf{x}, \mathbf{y})}{\partial x_2} \end{Bmatrix} = \frac{\sqrt{\Lambda}}{2\pi R^2} \begin{Bmatrix} r_1 \\ r_2 \end{Bmatrix}.$$

Particularly, the temperature fundamental solution (2.9) can reduce to the orthotropic and isotropic cases by simply setting  $k_{11} \neq k_{22}$ ,  $k_{12} = 0$  and  $k_{11} = k_{22}$ ,  $k_{12} = 0$ , respectively.

### 3. Hybrid finite element formulation

In this section, the  $n$ -sided polygonal element ( $n \geq 4$ ) is first used to solve the general anisotropic heat conduction problem. To achieve polygonal mesh division of a given domain, the Voronoi diagram can be employed. The Voronoi diagram is a fundamental polygonal geometrical subdivision of a given region, where the point set with more nearest neighbors can make up the vertices of the diagram [37, 38]. The quality of the generated polygonal mesh strongly depends on the distribution of scattered seeding points. In order to improve the quality of polygonal mesh to increase the accuracy of the solution, the centroidal Voronoi technique [39, 40] can be used, in which the seed point generating each Voronoi cell can be used as its center of mass. Figure 3 displays a polygonal mesh generated by the centroidal Voronoi technique in a complex L-shaped domain. For a particular polygonal element  $e$  displayed in Fig. 3, we need separately define an internal temperature field, a frame temperature field and a hybrid variation functional at element level.

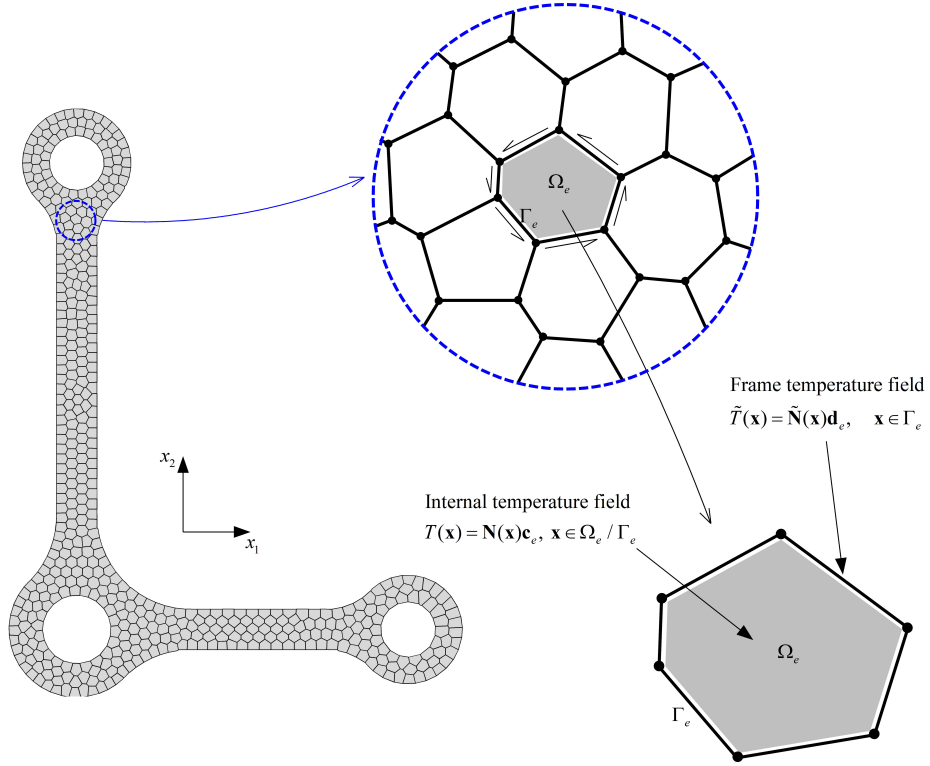


FIG. 3. Temperature approximations for a hybrid finite element.

### 3.1. Internal temperature field

The internal temperature field, also named as intra-element temperature field defined inside the element  $e$ , can be approximated by the linear combination of fundamental solutions with different source points  $\mathbf{y}_i$  ( $i = 1, \dots, m$ ), that is

$$(3.1) \quad T(\mathbf{x}) = \sum_{i=1}^m c_i T^*(\mathbf{x}, \mathbf{y}_i) = \mathbf{N}(\mathbf{x})\mathbf{c}_e, \quad \mathbf{x} \in \Omega_e / \Gamma_e, \mathbf{y}_i \notin \Omega_e$$

where  $m$  is the number of source points locating outside the element domain,  $c_i$  presents an unknown coefficient,  $T^*(\mathbf{x}, \mathbf{y}_i)$  is the temperature fundamental solution, and

$$(3.2) \quad \mathbf{N}(\mathbf{x}) = \{T^*(\mathbf{x}, \mathbf{y}_1) \ T^*(\mathbf{x}, \mathbf{y}_2) \ \dots \ T^*(\mathbf{x}, \mathbf{y}_m)\}, \quad \mathbf{c}_e = \{c_1 \ c_2 \ \dots \ c_m\}^T.$$

Next, differentiating the temperature field in Eq. (3.1) yields the following expression of the normal heat flux

$$(3.3) \quad q_n(\mathbf{x}) = \mathbf{Q}(\mathbf{x})\mathbf{c}_e$$

where

$$(3.4) \quad \mathbf{Q}(\mathbf{x}) = -\{n_1 \ n_2\} \begin{bmatrix} k_{11} & k_{12} \\ k_{21} & k_{22} \end{bmatrix} \begin{bmatrix} \frac{\partial \mathbf{N}(\mathbf{x})}{\partial x_1} \\ \frac{\partial \mathbf{N}(\mathbf{x})}{\partial x_2} \end{bmatrix}$$

with

$$(3.5) \quad \frac{\partial \mathbf{N}(\mathbf{x})}{\partial x_i} = \left\{ \frac{\partial T^*(\mathbf{x}, \mathbf{y}_1)}{\partial x_i} \quad \frac{\partial T^*(\mathbf{x}, \mathbf{y}_2)}{\partial x_i} \quad \dots \quad \frac{\partial T^*(\mathbf{x}, \mathbf{y}_m)}{\partial x_i} \right\}, \quad (i = 1, 2).$$

### 3.2. Frame temperature field

It is observed that the internal temperature approximation (3.1) is chosen so as to *a priori* satisfy the governing partial differential Eq. (2.1) inside the element domain. However, it is non-conforming across the inter-element boundary. To overcome this drawback, in this study, the hybrid technique is employed. In this technique, the element *e* is linked to adjacent elements through an auxiliary conforming frame field independently defined on the element boundary which has the same form as in the conventional FEM and BEM. Here, the frame temperature field  $\tilde{T}$  is given by

$$(3.6) \quad \tilde{T}(\mathbf{x}) = \tilde{\mathbf{N}}(\xi) \mathbf{d}_e, \quad \mathbf{x} \in \Gamma_e$$

where  $\tilde{\mathbf{N}}(\mathbf{x}) = [\tilde{\mathbf{N}}_1(\xi) \ \tilde{\mathbf{N}}_2(\xi) \ \dots \ \tilde{\mathbf{N}}_p(\xi)]$  is the shape function vector,  $\mathbf{d}_e = [T_1 \ T_2 \ \dots \ T_p]^T$  is the nodal temperature vector, *p* represents the number of nodes for the polygonal element, and  $-1 \leq \xi \leq 1$  is the local natural coordinate, which is related to the global coordinate  $\mathbf{x}$  on the element edge by the following expression in matrix form

$$(3.7) \quad \mathbf{x}(\xi) = \tilde{\mathbf{N}}(\xi) \mathbf{x}_e, \quad \mathbf{x} \in \Gamma_e$$

where  $\mathbf{x}_e$  is the nodal coordinate matrix

$$(3.8) \quad \mathbf{x}_e = \begin{bmatrix} \mathbf{x}_1^T \\ \mathbf{x}_2^T \\ \vdots \\ \mathbf{x}_p^T \end{bmatrix} = \begin{bmatrix} x_{11} & x_{12} \\ x_{21} & x_{22} \\ \vdots & \vdots \\ x_{p1} & x_{p2} \end{bmatrix}$$

and  $\mathbf{x} = [x_1 \ x_2]^T$ ,  $\mathbf{x}_i = [x_{i1} \ x_{i2}]^T$ .

For the *n*-sided polygonal element with *n* edges and *p* nodes, if there are two nodes on each edge, we have *p* = *n*. For such a case, the linear interpolation scheme is employed. For example, when the boundary point  $\mathbf{x}$  locates on the *i*th edge (*i* = 1, ..., *n* - 1),

$$(3.9) \quad \tilde{\mathbf{N}}_i(\xi) = \tilde{N}_1(\xi), \quad \tilde{\mathbf{N}}_{i+1}(\xi) = \tilde{N}_2(\xi), \quad \tilde{\mathbf{N}}_j(\xi) = 0 \quad (j \neq i, i + 1)$$

when the boundary point  $\mathbf{x}$  locates on the  $n$ th edge,

$$(3.10) \quad \tilde{\mathbf{N}}_n(\xi) = \tilde{N}_1(\xi), \quad \tilde{\mathbf{N}}_1(\xi) = \tilde{N}_2(\xi), \quad \tilde{\mathbf{N}}_j(\xi) = 0 \quad (j \neq n, 1)$$

where  $\tilde{N}_i$  ( $i = 1, 2$ ) stand for the conventional one-dimensional shape functions expressed in terms of the local natural coordinate  $\xi$ , that is

$$(3.11) \quad \tilde{N}_1(\xi) = \frac{1-\xi}{2}, \quad \tilde{N}_2(\xi) = \frac{1+\xi}{2} \quad (-1 \leq \xi \leq 1).$$

Certainly, a more accurate approximation of the frame temperature solution can be taken in Eq. (3.6) by quadratic shape functions on each element edge [19].

### 3.3. Element stiffness equation

To enforce the inter-element continuity, the following double-variable hybrid functional for the element  $e$  is defined by an integral form

$$(3.12) \quad \begin{aligned} \Pi_e = & -\frac{1}{2} \int_{\Omega_e} \left[ k_{11} \left( \frac{\partial T}{\partial x_1} \right)^2 + 2k_{12} \frac{\partial T}{\partial x_1} \frac{\partial T}{\partial x_2} + k_{22} \left( \frac{\partial T}{\partial x_2} \right)^2 \right] d\Omega \\ & - \int_{\Gamma_{qe}} \bar{q} \tilde{T} d\Gamma + \int_{\Gamma_e} q_n (\tilde{T} - T) d\Gamma - \frac{1}{2} \int_{\Gamma_{ce}} h_\infty (\tilde{T} - T_\infty)^2 d\Gamma \end{aligned}$$

where  $\Gamma_{qe} = \Gamma_q \cap \Gamma_e$  and  $\Gamma_{ce} = \Gamma_c \cap \Gamma_e$  are element segments related to the normal heat flux and convection.

With the Gauss divergence theorem

$$(3.13) \quad \int_{\Omega} \frac{\partial f}{\partial x_i} d\Omega = \int_{\Gamma} f n_i d\Gamma \quad (i = 1, 2)$$

for any smoothed function  $f$ , the hybrid functional (3.12) can be simplified as

$$(3.14) \quad \begin{aligned} \Pi_e = & \frac{1}{2} \int_{\Omega_e} \left( k_{11} \frac{\partial^2 T}{\partial x_1^2} + 2k_{12} \frac{\partial^2 T}{\partial x_1 \partial x_2} + k_{22} \frac{\partial^2 T}{\partial x_2^2} \right) T d\Omega \\ & - \int_{\Gamma_{qe}} \bar{q} \tilde{T} d\Gamma - \frac{1}{2} \int_{\Gamma_e} q_n T d\Gamma + \int_{\Gamma_e} q_n \tilde{T} d\Gamma - \frac{1}{2} \int_{\Gamma_{ce}} h_\infty (\tilde{T} - T_\infty)^2 d\Gamma \end{aligned}$$

which can be reduced to

$$(3.15) \quad \Pi_e = -\frac{1}{2} \int_{\Gamma_e} q_n T d\Gamma - \int_{\Gamma_{qe}} \bar{q} \tilde{T} d\Gamma + \int_{\Gamma_e} q_n \tilde{T} d\Gamma - \frac{1}{2} \int_{\Gamma_{ce}} h_\infty (\tilde{T} - T_\infty)^2 d\Gamma$$

by considering the fact that the approximated internal temperature field *priori* satisfies the governing equation.

Then, the substitution of Eqs. (3.1) and (3.6) into Eq. (3.15) yields

$$(3.16) \quad \Pi_e = -\frac{1}{2}\mathbf{c}_e^T \mathbf{H}_e \mathbf{c}_e - \mathbf{d}_e^T \mathbf{g}_e + \mathbf{c}_e^T \mathbf{G}_e \mathbf{d}_e - \frac{1}{2}\mathbf{d}_e^T \mathbf{F}_e \mathbf{d}_e + \mathbf{d}_e^T \mathbf{f}_e - \mathbf{a}_e$$

with

$$(3.17) \quad \begin{aligned} \mathbf{H}_e &= \int_{\Gamma_e} \mathbf{Q}^T \mathbf{N} d\Gamma, & \mathbf{G}_e &= \int_{\Gamma_e} \mathbf{Q}^T \tilde{\mathbf{N}} d\Gamma, & \mathbf{g}_e &= \int_{\Gamma_{qe}} \tilde{\mathbf{N}}^T \bar{q} d\Gamma \\ \mathbf{F}_e &= \int_{\Gamma_{ce}} h_\infty \tilde{\mathbf{N}}^T \tilde{\mathbf{N}} d\Gamma, & \mathbf{f}_e &= \int_{\Gamma_{ce}} h_\infty T_\infty \tilde{\mathbf{N}}^T d\Gamma, & \mathbf{a}_e &= \int_{\Gamma_{ce}} \frac{h_\infty T_\infty^2}{2} d\Gamma \end{aligned}$$

which can be evaluated by the standard one-dimensional Gaussian quadrature rules along the element boundary.

The minimization of the hybrid functional  $\Pi_e$  with respect to  $\mathbf{c}_e$  and  $\mathbf{d}_e$  respectively leads to

$$(3.18) \quad \begin{aligned} \frac{\partial \Pi_e}{\partial \mathbf{c}_e^T} &= -\mathbf{H}_e \mathbf{c}_e + \mathbf{G}_e \mathbf{d}_e = \mathbf{0}, \\ \frac{\partial \Pi_e}{\partial \mathbf{d}_e^T} &= \mathbf{G}_e^T \mathbf{c}_e - \mathbf{g}_e - \mathbf{F}_e \mathbf{d}_e + \mathbf{f}_e = \mathbf{0} \end{aligned}$$

from which one obtains the optional relationship between  $\mathbf{c}_e$  and  $\mathbf{d}_e$  for the enforcement of inter-element continuity on the common element boundary

$$(3.19) \quad \mathbf{c}_e = \mathbf{H}_e^{-1} \mathbf{G}_e \mathbf{d}_e$$

and the element stiffness equations

$$(3.20) \quad \mathbf{k}_e \mathbf{d}_e = \mathbf{g}_e - \mathbf{f}_e$$

where  $\mathbf{k}_e = \mathbf{G}_e^T \mathbf{H}_e^{-1} \mathbf{G}_e - \mathbf{F}_e$  is the symmetric element stiffness matrix.

Assembling the element stiffness equation (3.20) can give the final global stiffness equation with symmetric and sparse coefficient matrix, which can be solved for determining the nodal temperature vector  $\mathbf{d}_e$  after the specific nodal temperature constraint is introduced. Furthermore, the unknown coefficients  $\mathbf{c}_e$  can be obtained using Eq. (3.19).

### 3.4. Recovery of constant temperature mode

However, it is noticed that the constant temperature mode associated with a vanishing heat flux is fully discarded from the fundamental solution so that the

matrix  $\mathbf{H}_e$  is of full rank and keeps invertible [37]. Therefore, the temperature at any point inside the element  $e$  cannot be evaluated directly by Eq. (3.1). Here, to recover the discarded term in each element, Eq. (3.1) is modified as by adding a constant term  $c_0$

$$(3.21) \quad T(\mathbf{x}) = \mathbf{N}(\mathbf{x})\mathbf{c}_e + c_0$$

Following the general treatment in [41], the least square matching of  $T$  and  $\tilde{T}$  at  $n$  element nodes gives

$$(3.22) \quad \sum_{i=1}^n (\mathbf{N}\mathbf{c}_e + c_0 - \tilde{T})^2|_{\text{node } i} = \min$$

from which the stability term  $c_0$  can be determined as

$$(3.23) \quad c_0 = \frac{1}{n} \sum_{i=1}^n (\tilde{T} - \mathbf{N}\mathbf{c}_e)|_{\text{node } i}.$$

### 3.5. Generation of source points

From Eq. (3.20), it is observed that the inverse of the matrix  $\mathbf{H}_e$  has to be evaluated in the computation of the elementary stiffness matrix  $\mathbf{K}_e$ . The necessary condition for the matrix  $\mathbf{H}_e$  to be of full rank is that the number of approximating kernels in Eq. (3.1) should satisfy the following condition

$$(3.24) \quad m \geq n_{dof} - 1$$

where  $n_{dof}$  is the total number of degrees of freedom of the polygonal element, which is specially equal to the number of nodes  $p$  of the element for the heat conduction problem.

Practically, an optimal number of source points are chosen based on the number of nodes  $p$  of the polygonal element, that is  $m = p$ , so that the rank condition (3.24) can be automatically achieved for the heat conduction problem. For such a typical case, as indicated in Fig. 4, the simplest way to generate these source points is

$$(3.25) \quad \mathbf{y}_i = \mathbf{x}_i^b + \gamma(\mathbf{x}_i^b - \mathbf{x}_c), \quad i = 1, \dots, p$$

where  $\mathbf{x}_i^b$  is the coordinates of the boundary node  $i$  and  $\mathbf{x}_c$  is the coordinates of the central point of the element. Here, a dimensionless positive parameter  $\gamma$  is introduced to control the distance between the source point and the element boundary. For the polygonal element of interest, the location of centroid  $\mathbf{x}_c$  can be evaluated using

$$(3.26) \quad \mathbf{x}_c = \frac{1}{p} \sum_{i=1}^p \mathbf{x}_i^b.$$

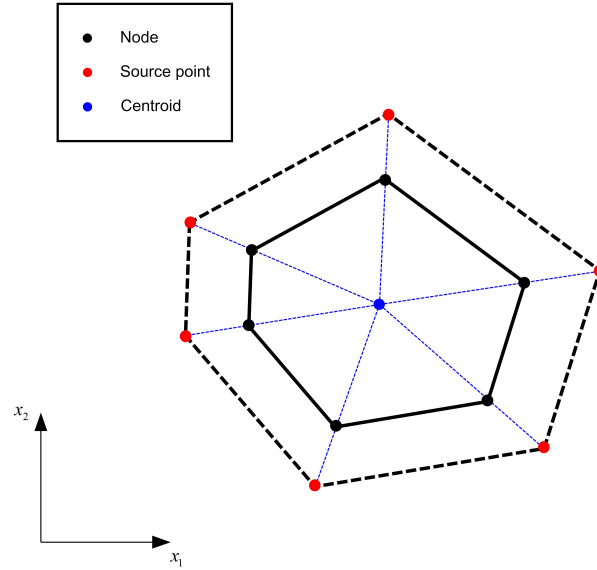


FIG. 4. Schematic of the generation of source points by element nodes.

#### 4. Numerical examples

In this section, some examples are solved to demonstrate the efficiency, accuracy and convergence properties of the present algorithm using *n*-sided hybrid finite elements. All physical quantities used have consistent units, i.e. the units of geometrical length, thermal conductivity, convection coefficient, temperature, heat flux, are m, W/(m · °C), W/(m<sup>2</sup> · °C), °C, W/m<sup>2</sup>, respectively. In order to properly assess the numerical results, the error norm or average relative error (Arerr) on an arbitrary smooth variable *f* is defined as

$$(4.1) \quad \text{Arerr}(f) = \sqrt{\frac{\sum_{i=1}^m (f_h - f_e)_i^2}{\sum_{i=1}^m (f_e)_i^2}},$$

where *m* is the number of test points in the computing domain, *f<sub>h</sub>* the hybrid finite element solution, and *f<sub>e</sub>* the exact solution.

##### 4.1. Anisotropic heat conduction in circular plate

In the first example, the anisotropic heat transfer in a unit circle is considered to test the accuracy, convergence and computing efficiency of the present method. The thermal conductivities of the anisotropic material are *k<sub>11</sub>* = 1, *k<sub>22</sub>* = 5,

$k_{12} = 2$ . Correspondingly, the exact solution of the problem is given by

$$(4.2) \quad T(x_1, x_2) = 3x_1^2 - x_2^2 + x_1x_2$$

which is also used to apply the temperature boundary condition on the circular boundary, as shown in Fig. 5.

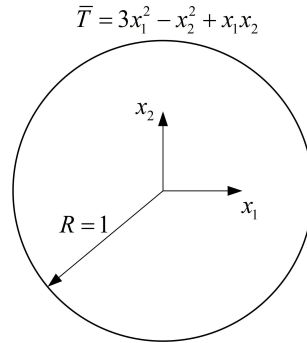


FIG. 5. The unit circular computing domain and the applied boundary conditions.

The circular region is modeled with 4-sided hybrid finite element firstly for the purpose of comparison to the conventional quadrilateral finite element. The number of 4-sided hybrid elements are 21, 46 and 150, which correspond to 28, 57 and 169 nodes, respectively, as indicated in Fig. 6. In the present hybrid element, one of open issues is the position of source points located outside the element. Figure 7 gives the variations of temperature norm at all nodes to the dimensionless parameter  $\gamma$  controlling the distance of source points to the element boundary, and it is observed that there are plateau stages to achieve steady results for all meshing schemes. In practical computation, the value of the dimensionless parameter  $\gamma$  can be taken to be 20 for the quadrilateral hybrid element.

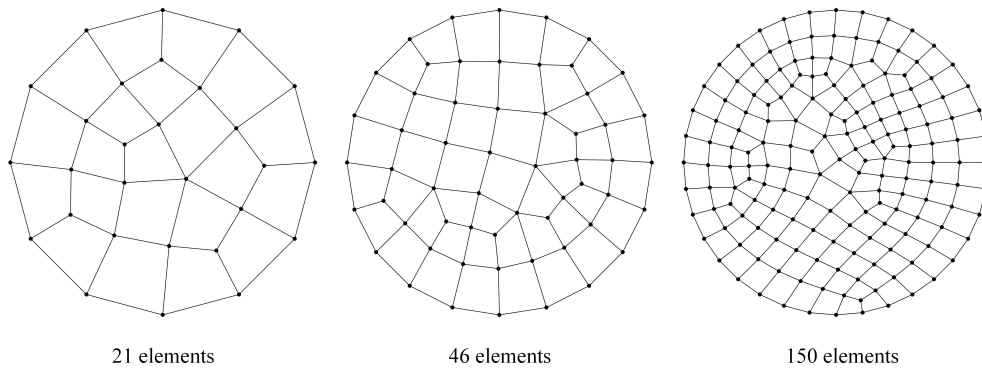


FIG. 6. Different divisions using quadrilateral hybrid elements for the circular region.

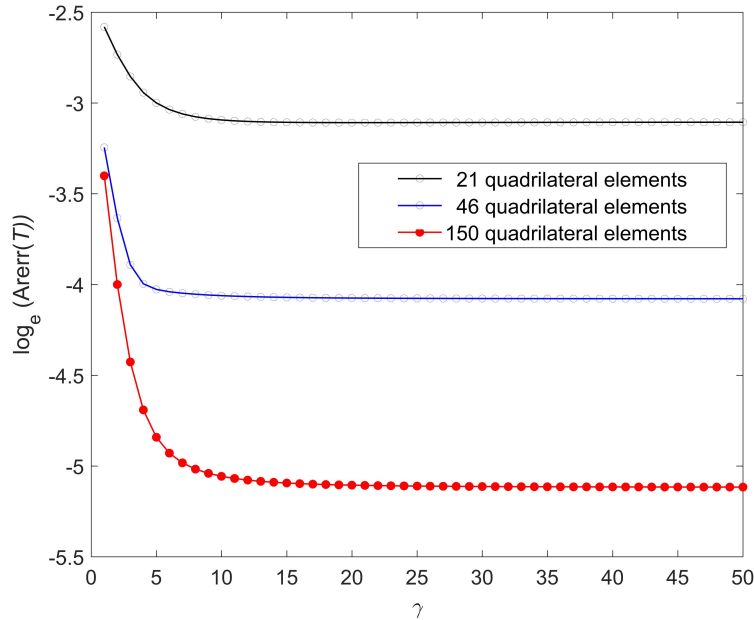


FIG. 7. Effect of the dimensionless parameter for quadrilateral hybrid elements.

Additionally, a good convergence is demonstrated in Fig. 7 as the error norm in temperature decreases with the increase of number of nodes. Subsequently, the results of temperature and heat flux components are tabulated in Table 1, from which it is indicated that the present hybrid finite element can produce better results of heat flux than the conventional finite element.

**Table 1. Comparison of results from the quadrilateral finite element and hybrid element.**

Elements	finite element			hybrid element		
	Arerr( <i>T</i> )	Arerr( <i>q</i> <sub>1</sub> )	Arerr( <i>q</i> <sub>2</sub> )	Arerr( <i>T</i> )	Arerr( <i>q</i> <sub>1</sub> )	Arerr( <i>q</i> <sub>2</sub> )
21	3.89E-2	2.13E-1	2.14E-1	4.18E-2	1.25E-1	1.28E-1
46	1.41E-2	1.18E-1	1.20E-1	1.69E-2	7.14E-2	7.40E-2
150	4.82E-3	5.92E-2	5.85E-2	5.00E-3	3.95E-2	4.11E-2

Apart from the quadrilateral hybrid element, another interesting issue of the present hybrid method is that the construction of polygonal element with arbitrary numbers of sides can be flexibly implemented without any difficulty. To illustrate this feature, the circular region is modeled using polygonal elements, as shown in Fig. 8. The number of nodes involved are 38, 90, 164 for the cases of 20, 46, 83 polygonal elements, respectively. Correspondingly, the variations of temperature norm are displayed in Fig. 9, from which it is seen that relatively steady results can be achieved when the value of the parameter  $\gamma$  exceeds 5.

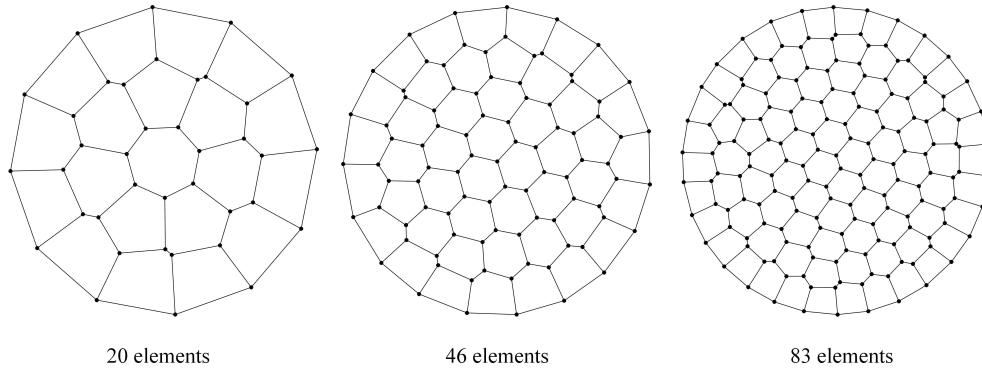


FIG. 8. Different divisions using polygonal hybrid elements for the circular region.

Moreover, a good convergence is observed in Fig. 9 with the increase of the number of elements. For performing more detailed investigation of convergence and computing efficiency, Figs. 10 and 11 displays the variations of error norm in temperature and heat flux component  $q_1$  against the total degrees of freedom (tdofs) of meshing. In Figs. 10 and 11, both the quadrilateral hybrid element and the polygonal hybrid element show good convergence in temperature and heat flux. Typically, in Fig. 10, the polygonal hybrid element shows slightly lower accuracy than the quadrilateral hybrid element. This can be attributed

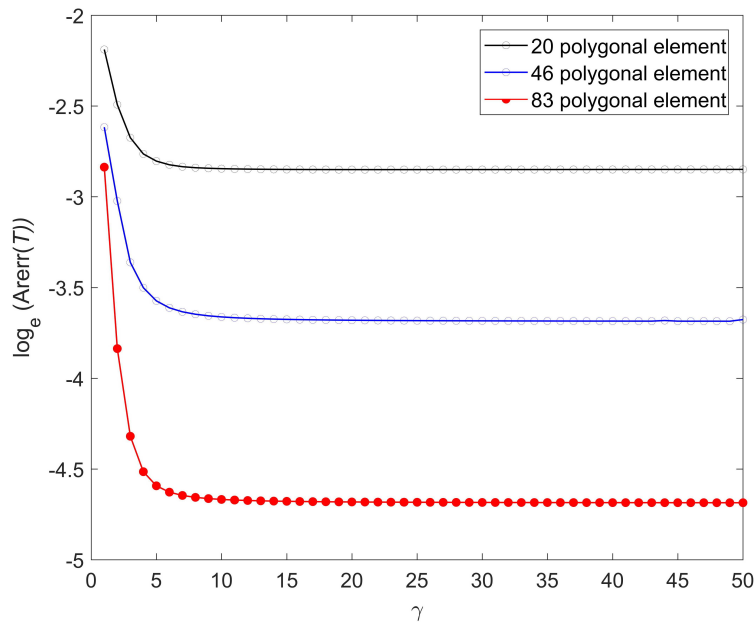


FIG. 9. Effect of the dimensionless parameter for polygonal hybrid elements.

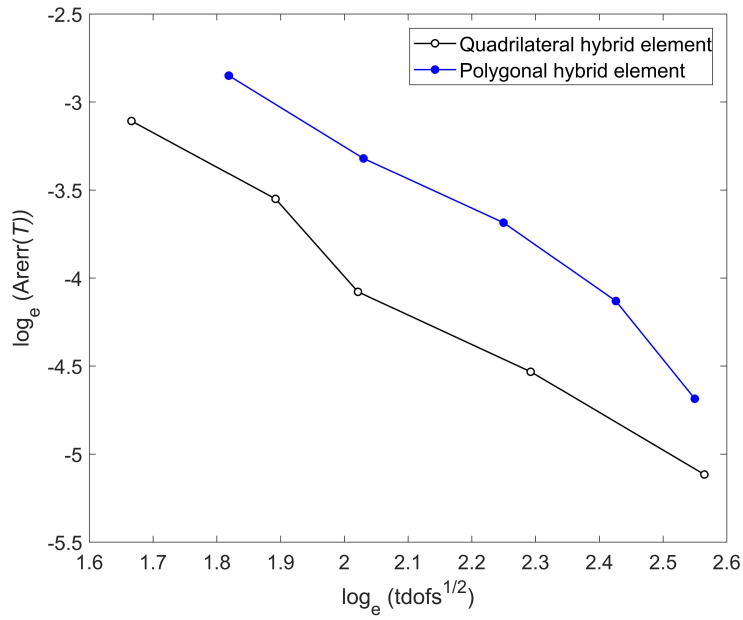


FIG. 10. Convergence results of the error norm in temperature for the present hybrid elements.

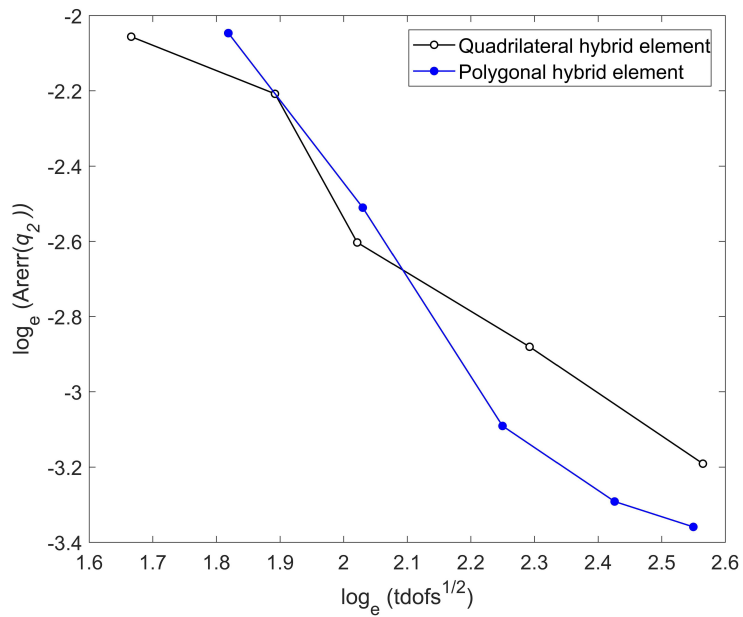


FIG. 11. Convergence results of the error norm in heat flux component for the present hybrid elements.

to the fact that the polygonal mesh possessing multiple-node connection feature includes less boundary nodes than the quadrilateral mesh when the same number of nodes are involved, so the variation of boundary conditions may not be fully captured for the polygonal mesh. For instance, the ratio of boundary nodes to all nodes, respectively, is 0.3158, 0.2111, 0.1829 only for the three polygonal meshes in Fig. 8, while it is 0.4286, 0.3509, 0.2130 for the quadrilateral meshes in Fig. 6. On the other hand, the quadrilateral and polygonal meshes in Fig. 10 have similar convergence rate (the average slope), which corresponds to 2.23, and 2.51, respectively. Comparatively, the convergence rate for the heat flux component in Fig. 11 is 1.28 and 1.79 for the quadrilateral and polygonal hybrid elements, respectively.

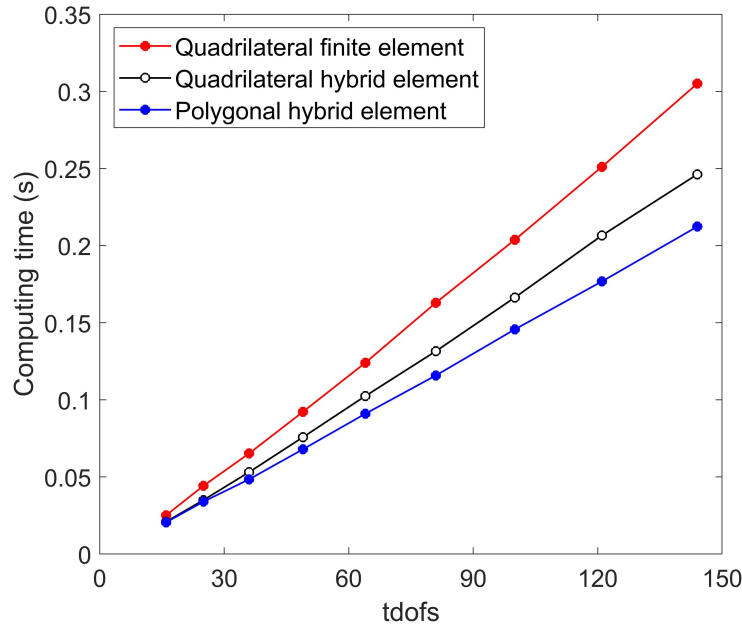


FIG. 12. Comparison of computing efficiency for finite element and hybrid element.

For the computing efficiency, which is illustrated by recording the computing time of the generation of global stiffness matrix, it is found in Fig. 12 that both the polygonal and quadrilateral hybrid elements are remarkably faster than the conventional finite element. This can be attributed to the element boundary integration scheme in the present method. Finally, the distributions of the temperature  $T$  and the heat flux component  $q_1$  are plotted in Fig. 13 when 83 polygonal hybrid finite elements are used. From Fig. 13, the very good agreements for temperature and heat flux distributions are observed between the numerical results and the exact solutions.

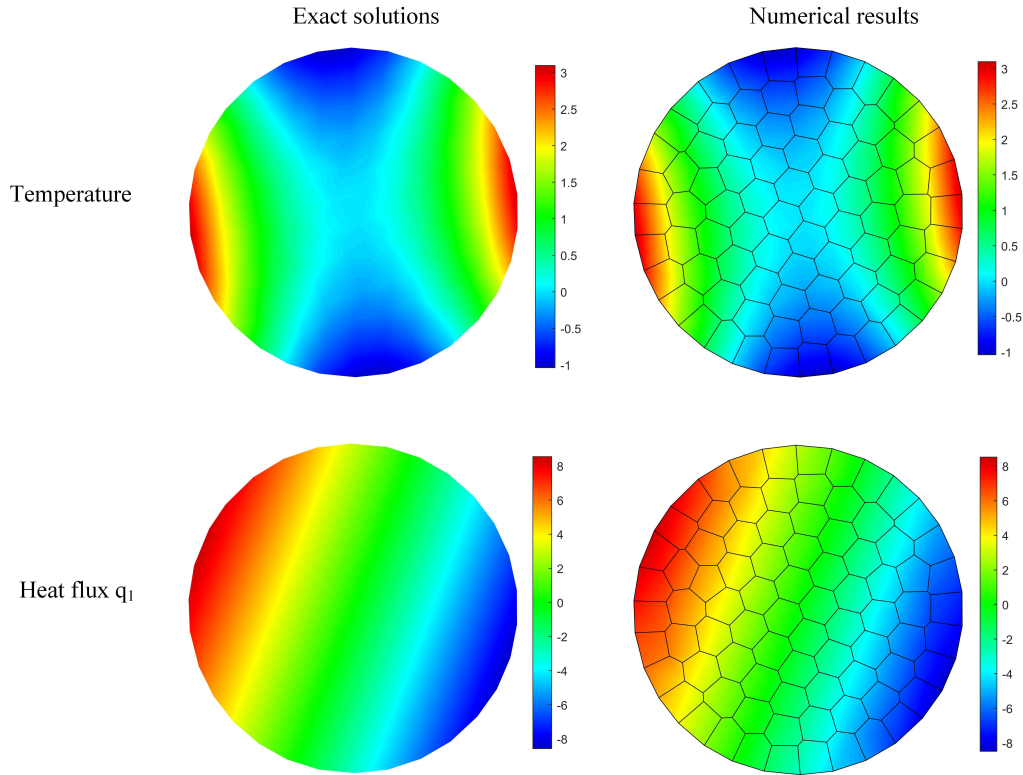


FIG. 13. Distributions of temperature and heat flux component in the circular region.

**4.2. Anisotropic heat conduction in square plate**

The second example is designed to investigate the capability of the present method over the non-convex elements and the non-conforming discretization in a unit square domain. Under the given anisotropic thermal conductivities  $k_{11} = 1$ ,  $k_{22} = 2$ ,  $k_{12} = 0$  and the specified temperature and heat flux boundary conditions (see Fig. 14), the solution of the problem is

$$(4.3) \quad T(x_1, x_2) = 2x_1^2 - x_2^2$$

which produces exact distribution of temperature in the square domain.

We now study a quantitative test where a non-convex polygon discretization in Fig. 15 is made in the square domain. The discretization includes four 8-sided polygons with 21 nodes. The parameter  $d$  is used to control the shape of non-convex polygons and the parameter  $a$  denotes the side length of a regular element. Typically, the polygons become regular when  $d/a = 0$ . Here, the result from the regular elements is taken as reference value. Correspondingly, the average relative

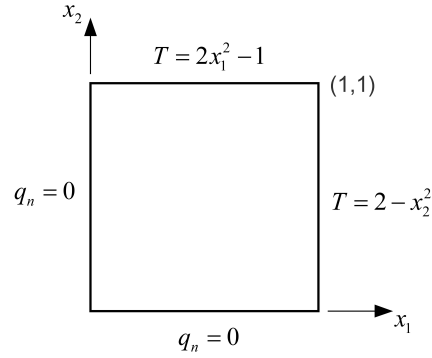


FIG. 14. The anisotropic square plate under specified boundary conditions.

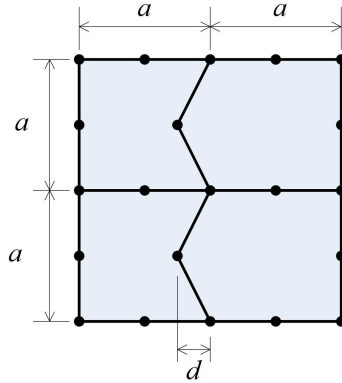


FIG. 15. Non-convex polygon discretization in the square.

error of temperature variabe for various  $d$  is listed in Table 2, from which very small deviations to the reference result are observed for all cases of non-convex polygones. Therefore, the present method can effectively handle the non-convex behavior of polygonal elements.

**Table 2. Comparison of non-convex and normal polygonal elements.**

$d/a$	0.0	0.2	0.4	0.6
$\text{Arerr}(T)$	0.01976	0.01996	0.01991	0.01974

Next the numerical convergence of the relative error in temperature norm is investigated by comparing the results from three mesh divisions, as shown in Fig. 16. Total 22, 42 and 62 nodes are involved for the three meshing configurations, including 12, 17 and 21 boundary nodes, respectively. The results of temperature in Fig. 17 show that relatively steady results can be achieved when

the value of the parameter  $\gamma$  exceeds 5. Moreover, it is seen from Fig. 17 that the numerical results from the present method converge to the exact solutions as the mesh is refined. To clearly demonstrate the rate of convergence in temperature, the logarithm relation of the total degrees of freedom (tdofs) of hybrid mesh and the relative error norm  $A_{err}(T)$  is plotted in Fig. 18, from which the average slope of the convergence line is evaluated as 1.71.

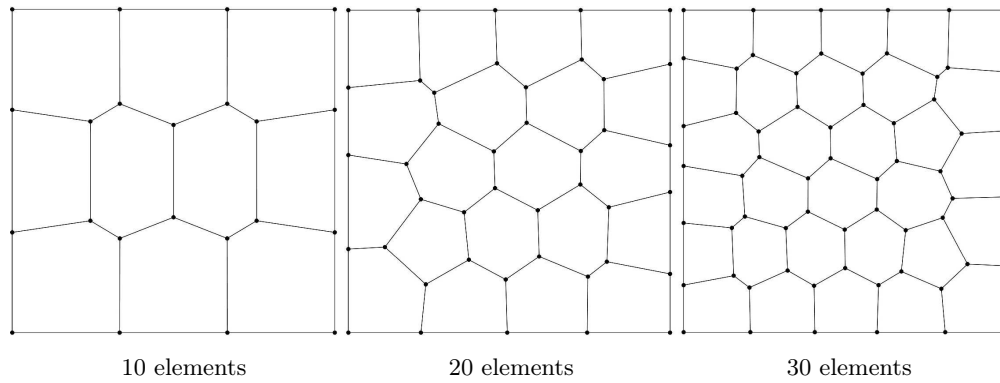


FIG. 16. Three divisions using polygonal hybrid elements for the square region.

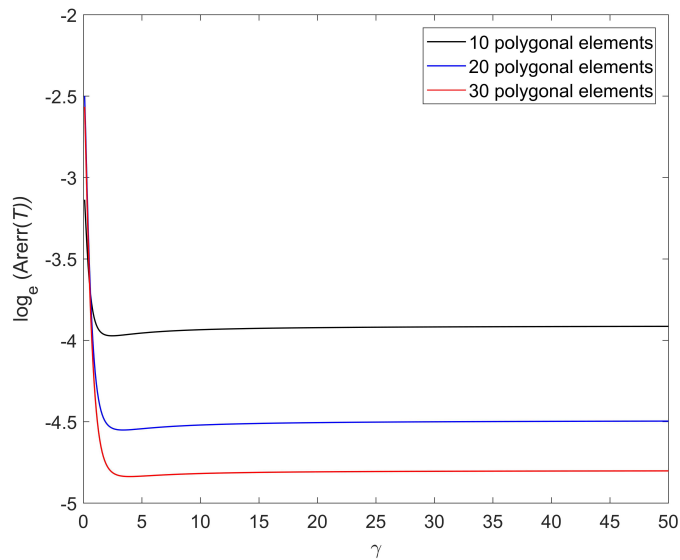


FIG. 17. Effect of the dimensionless parameter for polygonal hybrid elements.

Subsequently, an assessment of non-conforming discretization is carried out in the implementation of the present method, which has a clear edge over the

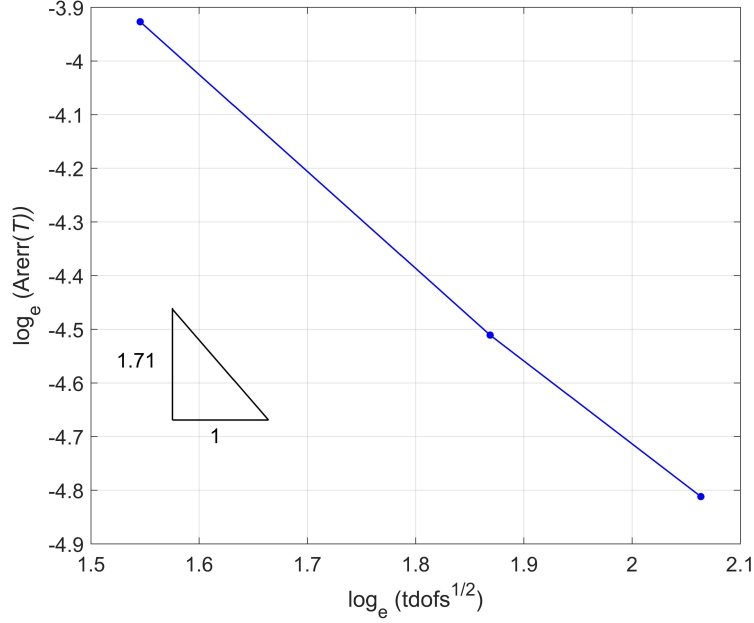


FIG. 18. Rate of convergence in temperature for the present polygonal hybrid element in Example 2.

conventional FEM in this aspect. Figure 19 shows a non-conforming discretization generated by applying the polytree rule [42] to the initial polygonal mesh including 20 elements and 42 nodes, in which a *father* element with  $n$  nodes is subdivided into  $n + 1$  *children* elements, and then each new element can be divided again to generate other children elements. In Fig. 19, the blue points denote the newly generated interior and hanging nodes and the hanging nodes are defined at the intersection between element edges. For such a non-conforming mesh, the HFS-FEM employs a more straightforward and normal way to handle the elements containing hanging nodes. In the HFS-FEM, a hanging node is simply understood as a subdivision of an edge, and as a result, the element including  $m$  hanging nodes and  $n$  nodes is regarded as a normal element with  $(n+m)$  nodes, and the element boundary integrals in the element stiffness matrix are normally evaluated edge by edge without any special treatment. With the locally refined mesh in Fig. 19, the model is solved with  $\gamma = 15$  and the relative error norms of temperature  $T$  and heat flux component  $q_1$  are 0.0101 and 0.0648, respectively, which are smaller than the reference results 0.0110 and 0.0919 from the initial mesh, as expected. Finally, the temperature distribution in the square domain is plotted in Fig. 20 with 30 polygonal elements in Fig. 16, and it is found that the numerical results show a great agreement with the exact solutions. Also,

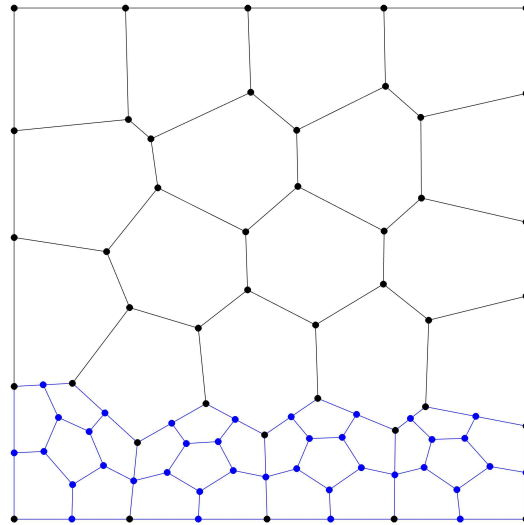


FIG. 19. Non-conforming polzgon discretiyation in the square.

in order to demonstrate the applicability of the present method for treating the convection condition, the left side of the square is changed into a convective side with a convection coefficient 50 and an environmental temperature 25. With the locally refined mesh division developed based on the 30 polygonal elements given in Fig. 16, the temperature distribution is plotted in Fig. 21, from which it is observed that the simulated results from the HFS-FEM show good compliance with the reference results from ABAQUS with 400 linear quadrilateral elements.

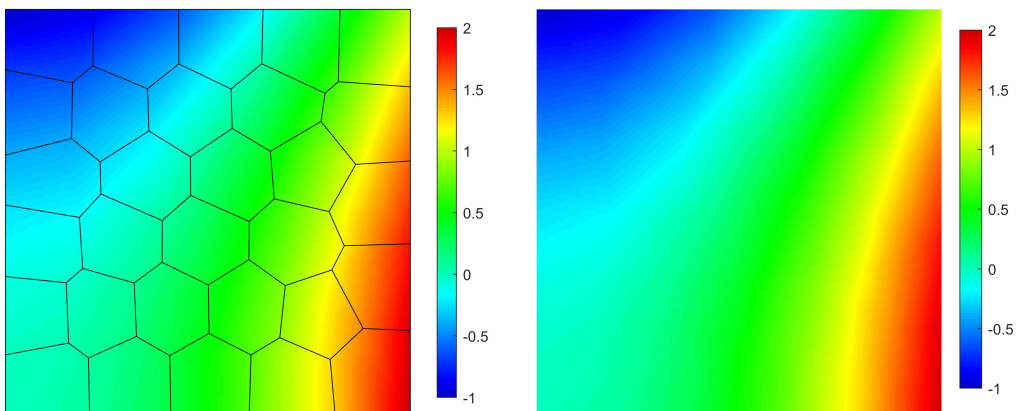


FIG. 20. Temperature distributions from the numerical (left) and exact (right) results in the square.

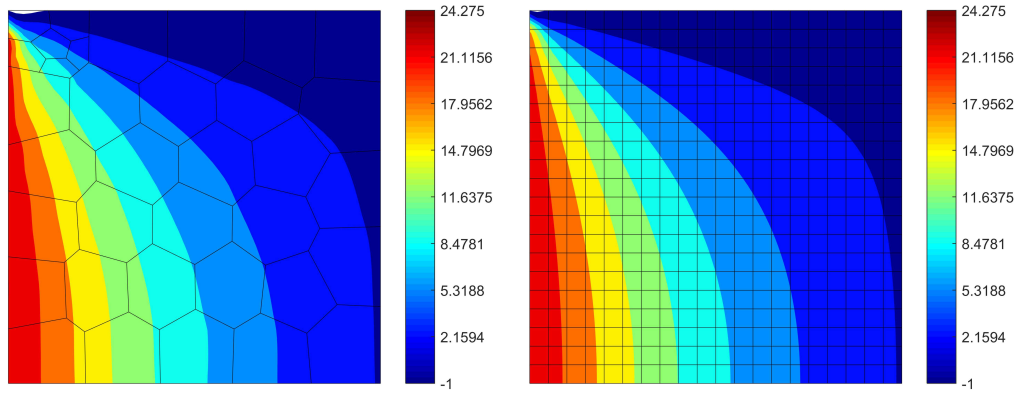


FIG. 21. Temperature distributions from the simulated (left) and reference (right) results in the square with applied convection condition.

#### 4.3. Anisotropic heat conduction in plane hook domain

As a final example, a relatively complex anisotropic hook plate is modelled to validate the capability of the HFS-FEM to handle a complex structure with

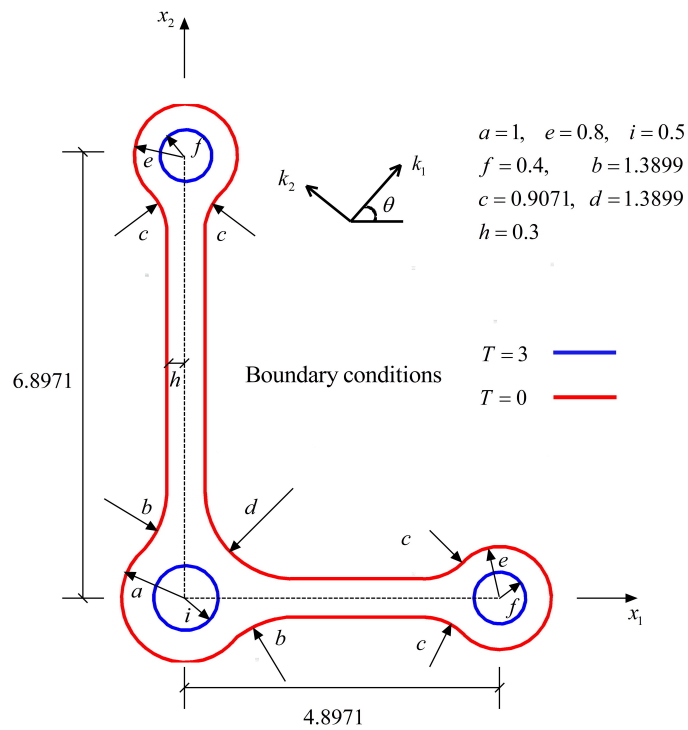


FIG. 22. Anisotropic plane hook domain.

*n*-sided polygonal elements. As shown in Fig. 22, the temperature boundary condition is assumed as  $T = 0$  on the outer face and  $T = 3$  on the inner face,

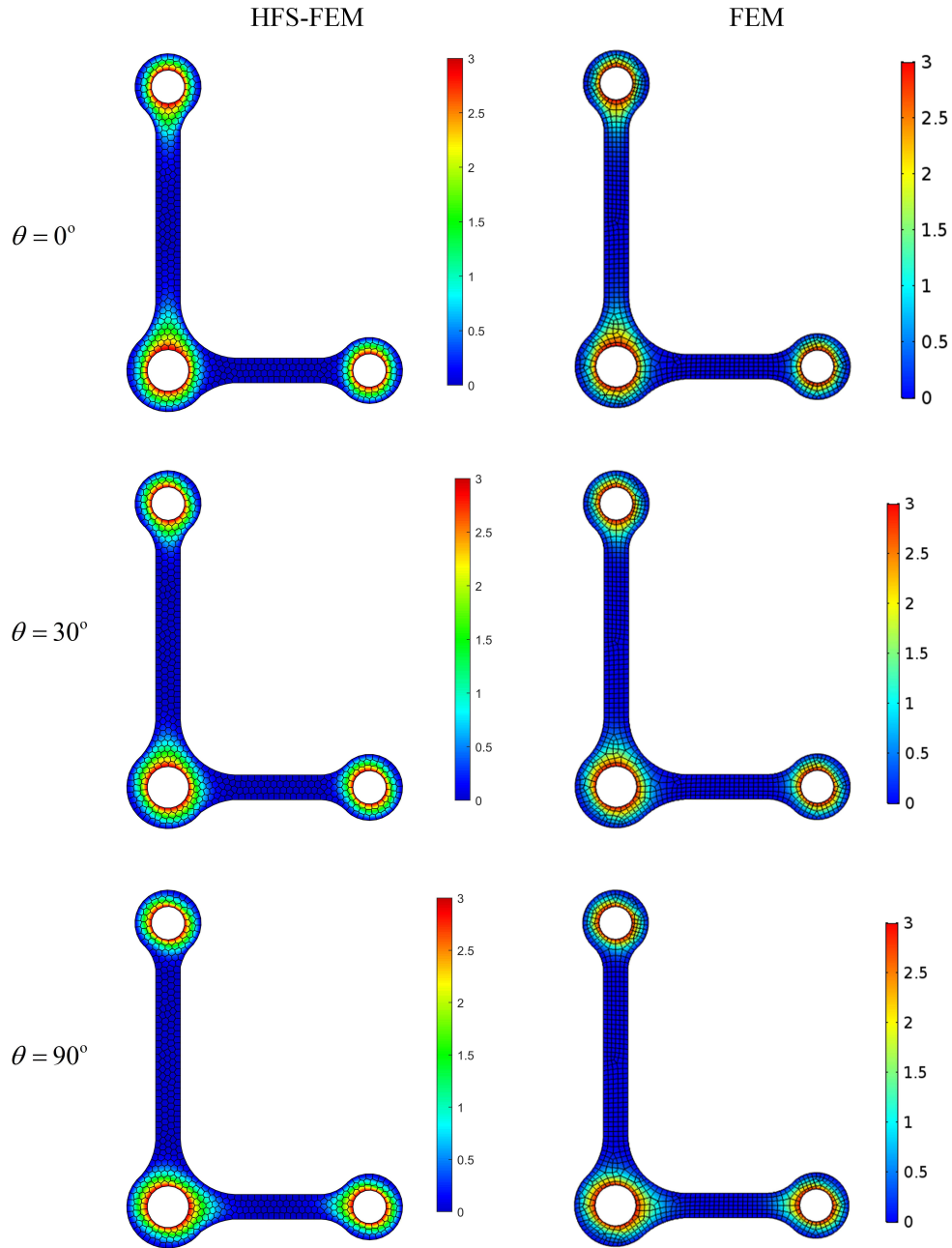


FIG. 23. The caused temperature distributions in the hook region for different ply angles.

respectively. The given orthotropic material parameters are  $k_1 = 1$  and  $k_2 = 5$ , thus the anisotropy of model can be represented by the ply angle  $\theta$  in Eq. (2.5). In this calculation, the hook domain is modeled with 500 polygonal elements and 1026 nodes. Moreover, the finite element solutions from ABAQUS are provided for comparison, in which the hook region is discretized with 600 quadrilateral elements and 1028 nodes. The color maps of temperature distribution are shown in Fig. 23 for different ply angles and it is observed that the numerical results from the HFS-FEM show a good compliance with the FEM results.

## 5. Conclusions

In this manuscript, the properties of accuracy, convergence, computational efficiency and easiness for treating non-convex and non-conforming mesh are studied for the present polygonal hybrid finite element method in the context of two-dimensional anisotropic heat conduction. In this method, the anisotropic fundamental solutions of the problem are employed for approximating an element interior temperature field in order to exactly satisfy the governing equation of problem, while one-dimensional linear shape functions are used for approximating element frame temperature field to enforce the continuity across the element boundary and the specified boundary conditions. As a result, this method involving element boundary integrals only permits to construct arbitrary polygonal elements with more sides to discretize complex computing domain, regardless of the types of polygonal elements, i.e. those with non-convex shapes and/or non-conforming connections. Numerical experiments demonstrate such features of this polygonal-mesh based technique.

It can be concluded that (1) The HFS-FEM with polygon discretization is practically applicable for two-dimensional anisotropic heat conduction; (2) Compared to the conventional FEM, the HFS-FEM has higher accuracy for heat flux component; (3) Both the quadrilateral hybrid elements and the polygonal hybrid elements exhibit better computing efficiency than the conventional finite element; (4) The method shows certain insensitivity to non-convex mesh; (5) The method exhibits great capability to exploit non-conforming mesh to reduce remeshing effort, which is typically important for crack propagation.

However, compared to the mostly known FEM, we have to point out that the present method is strongly dependent of fundamental solutions of problem, so it is not applicable to those without explicit expressions of fundamental solutions. Also, special treatment is typically required for inhomogeneous heat transfer problems, i.e. transient heat transfer and/or coupled thermo-mechanical processes, by introducing radial basis functions at element level for inhomogeneous term. This will be extendedly studied in the future. Actually, we think that the most appealing feature of the present method is the applicability of special

polygonal element for homogeneous problems, as demonstrated in [20–23, 25], rather than for inhomogeneous problems.

## Acknowledgements

The research was funded by the Program for Innovative Research Team of Science & Technology of Henan Province of China (No. 19IRTSTHN020).

## References

1. K.A. WOODBURY, H. NAJAFI, J.V. BECK, *Exact analytical solution for 2-D transient heat conduction in a rectangle with partial heating on one edge*, International Journal of Thermal Sciences, **112**, 252–262, 2017.
2. R.L. MCMASTERS, J.V. BECK, *A two-dimensional cylindrical transient conduction solution using green's functions*, Journal of Heat Transfer, **136**, 10, 101301 (8 pages), 2014.
3. K.D. COLE, D.H.Y. YEN, *Green's functions, temperature and heat flux in the rectangle*, International Journal of Heat and Mass Transfer, **44**, 20, 3883–3894, 2001.
4. H. GU, J.F. HUNT, *Two-dimensional finite element heat transfer model of softwood. Part II. Macrostructural effects*, Wood Science and Technology, **38**, 4, 599–608, 2006.
5. M. TRCALA, *A 3D transient nonlinear modelling of coupled heat, mass and deformation fields in anisotropic material*, International Journal of Heat and Mass Transfer, **55**, 17–18, 4588–4596, 2012.
6. M.I. AZIS, D.L. CLEMENTS, *Nonlinear transient heat conduction problems for a class of inhomogeneous anisotropic materials by BEM*, Engineering Analysis with Boundary Elements, **32**, 12, 1054–1060, 2008.
7. S. ISHIGURO, H. NAKAJIMA, M. TANAKA, *Analysis of two-dimensional steady-state heat conduction in anisotropic solids by boundary element method using analog equation method and Green's theorem*, Transactions of the Japan Society of Mechanical Engineers, Series A, **74**, 740, 477–483, 2008.
8. F.J. WANG, Q.S. HUA, C.S. LIU, *Boundary function method for inverse geometry problem in two-dimensional anisotropic heat conduction equation*, Applied Mathematics Letters, **84**, 130–136, 2018.
9. N. SALAM, A. HADDADE, D.L. CLEMENTS, M.I. AZIS, *A boundary element method for a class of elliptic boundary value problems of functionally graded media*, Engineering Analysis with Boundary Elements, **84**, 186–190, 2017.
10. H. WANG, Q.H. QIN, Y.L. KANG, *A meshless model for transient heat conduction in functionally graded materials*, Computational Mechanics, **38**, 1, 51–60, 2005.
11. J. SLADEK, V. SLADEK, P.H. WEN, B. HON, *Inverse heat conduction problems in three-dimensional anisotropic functionally graded solids*, Journal of Engineering Mathematics, **75**, 1, 157–171, 2012.
12. J.P. ZHANG, G.Q. ZHOU, S.G. GONG, S.S. WAN, *Transient heat transfer analysis of anisotropic material by using element-free Galerkin method*, International Communications in Heat and Mass Transfer, **84**, 134–143, 2017.

13. J. JIROUSEK, Q.H. QIN, *Application of hybrid-Trefftz element approach to transient heat conduction analysis*, Computers & Structures, **58**, 195–201, 1996.
14. Q.H. QIN, *Trefftz Finite and Boundary Element Method*, WIT Press, Southampton, 2000.
15. S. LU, J. LIU, G. LIN, P. ZHANG, *Modified scaled boundary finite element analysis of 3D steady-state heat conduction in anisotropic layered media*, International Journal of Heat and Mass Transfer, **108**, 2462–2471, 2017.
16. N. SUKUMAR, A. TABARRAEI, *Conforming polygonal finite elements*, International Journal for Numerical Methods in Engineering, **61**, 12, 2045–2066, 2004.
17. A. TABARRAEI, N. SUKUMAR, *Application of polygonal finite elements in linear elasticity*, International Journal of Computational Methods, **3**, 4, 503–520, 2006.
18. G. MANZINI, A. RUSSO, N. SUKUMAR, *New perspectives on polygonal and polyhedral finite element methods*, Mathematical Models and Methods in Applied Sciences, **24**, 8, 1665–1699, 2014.
19. H. WANG, Q.H. QIN, *Hybrid FEM with fundamental solutions as trial functions for heat conduction simulation*, Acta Mechanica Solida Sinica, **22**, 5, 487–498, 2009.
20. H. WANG, Q.H. QIN, *Fundamental-solution-based hybrid FEM for plane elasticity with special elements*, Computational Mechanics, **48**, 5, 515–528, 2011.
21. H. WANG, Q.H. QIN, *Boundary integral based graded element for elastic analysis of 2D functionally graded plates*, European Journal of Mechanics – A/Solids, **33**, 12–23, 2012.
22. H. WANG, Q.H. QIN, *A new special element for stress concentration analysis of a plate with elliptical holes*, Acta Mechanica, **223**, 6, 1323–1340, 2012.
23. H. WANG, Q.H. QIN, *A new special coating/fiber element for analyzing effect of interface on thermal conductivity of composites*, Applied Mathematics and Computation, **268**, 311–321, 2015.
24. H. WANG, Q.H. QIN, C.Y. LEE, *n-sided polygonal hybrid finite elements with unified fundamental solution kernels for topology optimization*, Applied Mathematical Modelling, **66**, 97–117, 2019.
25. H. WANG, Q.-H. QIN, Y. XIAO, *Special n -sided Voronoi fiber/matrix elements for clustering thermal effect in natural-hemp-fiber-filled cement composites*, International Journal of Heat and Mass Transfer, **92**, 228–235, 2016.
26. H. WANG, Q.H. QIN, *Fundamental-solution-based finite element model for plane orthotropic elastic bodies*, European Journal of Mechanics – A/Solids, **29**, 5, 801–809, 2010.
27. H. WANG, Q.H. QIN, *A fundamental solution-based finite element model for analyzing multi-layer skin burn injury*, Journal of Mechanics in Medicine and Biology, **12**, 5, 1250027, 2012.
28. Z. SHE, K.Y. WANG, P.C. LI, *Hybrid Trefftz polygonal elements for heat conduction problems with inclusions/voids*, Computers & Mathematics with Applications, 2019.
29. Z. SHE, K.Y. WANG, P.C. LI, *Thermal analysis of multilayer coated fiber-reinforced composites by the hybrid Trefftz finite element method*, Composite Structures, **224**, 110992, 2019.
30. K.Y. WANG, P.C. LI, D.Z. WANG, *Trefftz-type FEM for solving orthotropic potential problems*, Latin American Journal of Solids and Structures, **11**, 2537–2554, 2014.

31. J.C. ZHOU, K.Y. WANG, P.C. LI, *A hybrid fundamental-solution-based 8-node element for axisymmetric elasticity problems*, Engineering Analysis with Boundary Elements, **101**, 297–309, 2019.
32. J.C. ZHOU, K.Y. WANG, P.C. LI, *Hybrid fundamental solution based finite element method for axisymmetric potential problems with arbitrary boundary conditions*, Computers & Structures, **212**, 72–85, 2019.
33. J.C. ZHOU, K.Y. WANG, P.C. LI, X.D. MIAO, *Hybrid fundamental solution based finite element method for axisymmetric potential problems*, Engineering Analysis with Boundary Elements, **91**, 82–91, 2018.
34. O.C. ZIENKIEWICZ, R.L. TAYLOR, J.Z. ZHU, *The Finite Element Method: Its Basic and Fundamentals*, Elsevier, New York, 2005.
35. F.C. BURONI, R.J. MARCZAK, M. DENDA, A. SÁEZ, *A formalism for anisotropic heat transfer phenomena: foundations and Green's functions*, International Journal of Heat and Mass Transfer, **75**, 399–409, 2014.
36. R.J. MARCZAK, M. DENDA, *New derivations of the fundamental solution for heat conduction problems in three-dimensional general anisotropic media*, International Journal of Heat and Mass Transfer, **54**, 15, 3605–3612, 2011.
37. F. AURENHAMMER, R. KLEIN, D.T. LEE, *Voronoi Diagrams and Delaunay Triangulations*, World Scientific, Singapore, 2013.
38. A. OKABE, B. BOOTS, K. SUGIHARA, S.N. CHIU, D.G. KENDALL, *Spatial Tessellations: Concepts and Applications of Voronoi Diagrams*, Wiley, Boston, 2000.
39. Q. DU, D. WANG, *Anisotropic centroidal Voronoi tessellations and their applications*, SIAM Journal on Scientific Computing, **26**, 3, 737–761, 2005.
40. Q. DU, V. FABER, M. GUNZBURGER, *Centroidal Voronoi tessellations: applications and algorithms*, SIAM Review, **41**, 4, 637–676, 1999.
41. Q.H. QIN, *The Trefftz Finite and Boundary Element Method*, WITpress Boston, Southampton, 2000.
42. K.N. CHAU, K.N. CHAU, T. NGO, K. HACKL, H. NGUYEN-XUAN, *A polytree-based adaptive polygonal finite element method for multi-material topology optimization*, Computer Methods in Applied Mechanics and Engineering, **332**, 712–739, 2018.

Received November 21, 2019; revised version March 15, 2020.

Published online April 30, 2020.

---

